Title
Influence of magnetic field configuration on magnetohydrodynamic waves in Earth's core

Authors
Knezek, Nicholas
Buffett, Bruce

Publication Date
2018-04-01

DOI
10.1016/j.pepi.2018.01.005

Peer reviewed

Physics of the Earth and Planetary Interiors 277 (2018) 1–9

Contents lists available at ScienceDirect

Physics of the Earth and Planetary Interiors

journal homepage: www.elsevier.com/locate/pepi

Influence of magnetic field configuration on magnetohydrodynamic waves in Earth's core

Nicholas Knezek*, Bruce Buffett

Dept. of Earth and Planetary Science, University of California Berkeley, United States

A B S T R A C T

We develop a numerical model to study magnetohydrodynamic waves in a thin layer of stratified fluid near the surface of Earth's core. Past studies have been limited to using simple background magnetic field configurations. However, the choice of field distribution can dramatically affect the structure and frequency of the waves. To permit a more general treatment of background magnetic field and layer stratification, we combine finite volume and Fourier methods to describe the wave motions. We validate our model by comparisons to previous studies and examine the influence of background magnetic field configuration on two types of magnetohydrodynamic waves. We show that the structure of zonal Magnetic-Archimedes-Coriolis (MAC) waves for a dipole background field is unstable to small perturbations of the field strength in the equatorial region. Modifications to the wave structures are computed for a range of field configurations. In addition, we show that non-zonal MAC waves are trapped near the equator for realistic magnetic field distributions, and that their latitudinal extent depends upon the distribution of magnetic field strength at the CMB.

1. Introduction

Earth's geomagnetic field originates due to motions in Earth's liquid outer core. Despite decades of study, many aspects of the large-scale dynamics of the core are uncertain. In particular, it is possible that the topmost region of the outer core is stably stratified and does not participate in convection with the rest of the core fluid. Many authors have claimed to detect such a layer using seismic (Tanaka, 2007) or geomagnetic evidence (Whaler, 1980; Lesur et al., 2015), but its existence remains in dispute. Changes in Earth's internal magnetic field, termed geomagnetic secular variation (GSV), originate due to fluid motions near the core surface and can be used to study the dynamics of fluid in this region (Holme and Whaler, 2001; Livermore et al., 2016). In particular, periodic fluctuations in GSV have been attributed to magnetohydrodynamic waves in Earth's core, which can constrain properties such as the strength of the core's internal magnetic field (Hide, 1966; Hori et al., 2015) or the thickness and strength of buoyancy of the proposed stratified layer (Buffett, 2014). These techniques are becoming increasingly powerful due to active satellite missions which enable high-resolution observations of GSV (Finlay et al., 2016), and several authors have already claimed to detect previously unobserved propagating waves and fluid motions using satellite observations (Chulliat et al., 2015; Livermore et al., 2016).

To obtain useful constraints on physical properties of the core from periodic signals in the GSV, the structure of magnetohydrodynamic waves and their dependence on various core properties must be derived through analytical or numerical techniques. Past studies have used simplified models of the core's internal field such as a pure dipole (Braginsky, 1993) or axially-aligned field (Vidal and Schaeffer, 2015) to simplify the description of the problem. However, observations of Earth's core field (Jackson et al., 2000) and the latest high-resolution numerical dynamo models (Schaeffer et al., 2017) indicate that the true field in the core is likely to be have a more complicated structure. Because these waves depend on the internal magnetic field to propagate, the configuration of the background magnetic field can heavily influence their period and spatial structure and therefore dramatically influence the interpretation of observations.

Analytical derivations of waves modes in Earth's core typically retain only a simplified description of the field. Braginsky (1993) and Bergman (1993) use the radial component of a pure dipole field to derive the structure of Magnetic-Archimedes-Coriolis (MAC) waves and equatorially-trapped Rossby waves in a stratified layer near the CMB. Both authors find the strongest fluid motions near the equator, where the dipole approximation has no radial component. However, the observed geomagnetic field has a significant radial component in this region (Jackson et al., 2000), so it would be reasonable to question at least some of the conclusions of these studies. Hide (1966), in contrast, uses a beta-plane approximation to derive slow Rossby waves in the

* Corresponding author.
E-mail address: nknezek@gmail.com (N. Knezek).

https://doi.org/10.1016/j.pepi.2018.01.005
Received 17 August 2017; Received in revised form 6 December 2017; Accepted 8 January 2018
Available online 12 January 2018
0031-9201/

bulk of the core with a purely toroidal field where $\overrightarrow{B}(r,\theta,\phi) = B_0 r\sin\theta\hat{\phi}$, sometimes referred to as the Malkus field. The Malkus field increases steadily with radial distance from the rotation axis and has its strongest value in the equatorial region at the CMB. From physical arguments, Braginsky (1993) and Bergman (1993) argue that the toroidal field should be small near the CMB, and recent high-resolution numerical dynamo simulations support this claim (Schaeffer et al., 2017), so the Malkus field may not be a suitable approximation for the region close to the CMB.

Numerical solutions have the potential to overcome the limitations imposed by analytical techniques, permitting studies with more general background field configurations. However, numerical studies often use fields similar to those used in analytical derivations. Vidal and Schaeffer (2015) use the Malkus field and an axially-aligned field $\overrightarrow{B}(r,\theta,\phi) = B_0\hat{z}$ to confirm that fast MC waves are largely unaffected by the background magnetic field. More relevant to this work, Márquez-Artavia et al. (2017) uses a simple toroidal field $\overrightarrow{B}(r,\theta,\phi) = B_0\sin\theta\hat{\phi}$ to examine magnetic shallow water waves on a sphere. Buffett (2014) derived solutions for MAC waves with both a constant radial field $\overrightarrow{B}(r,\theta,\phi) = B_0\hat{r}$ and a vertical field, finding very different wave structures for each (see Buffett, 2014, Fig. 2 and Extended Data Fig. 1). All of these studies used spherical harmonics to describe the field and layer structures when formulating the eigenvalue problem for the waves. Spherical harmonic expansions are commonly used to study waves in Earth's core and are numerically efficient for simple background field configurations. However, the complexity of the computations increase severely with more general descriptions of the background magnetic field due to coupling between modes which necessarily lead to dense matrix equations that are computationally expensive to solve. This has limited the study of more complex background magnetic fields, despite the fact that the choice of background field likely has a large influence on wave structures and on the interpretation of geomagnetic observations.

In order to understand the influence of background magnetic field configuration on waves in stratified layers, we develop a new flexible numerical model that utilizes a hybrid finite-volume and Fourier eigenvalue method. A finite-volume formulation allows us to efficiently study wave dynamics with complex background magnetic fields while using only sparse matrices. Finite volume methods also avoid numerical singularities at the north and south poles that arise with finite difference methods and may also simplify coupling the spherical shell layer presented in this work to the non-spherical structure of geostrophic motion in the bulk core in future work. We choose not to adopt a finite-element approach because our domain is regular and so we can avoid the extra numerical overhead required to track connectivity of elements. A linearized description of the waves allows for Fourier decomposition of the problem into individual azimuthal wave modes, as modes do not couple to each other when the background magnetic field and layer buoyancy are axially-symmetric, which is assumed throughout this paper. We combined these ingredients to formulate an eigenvalue problem for the wave motion and obtain solutions for the wave structures, periods, and quality factors.

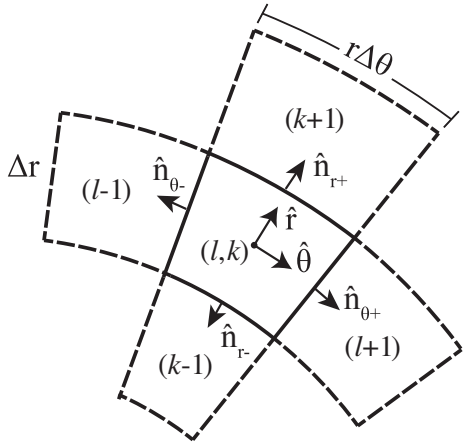

Fig. 1. Finite-volume cell geometry. Dimensions exaggerated for illustration purposes.

2. Model formulation

We compute the velocity ($\vec{V}$), magnetic field ($\overrightarrow{B}$), pressure (P), and radial displacement (U_r) for waves in the thin layer. The evolution of these variables are determined by a set of governing equations derived from the Navier–Stokes equations for velocity, the induction equation for magnetic field, and mass continuity equations for pressure and radial displacement. These equations are discretized using a hybrid finite volume and Fourier (FVF) method. Finally, the equations are linearized and wave solutions are obtained by using a sparse-matrix eigenvalue solver.

2.1. Governing equations

We adopt the Boussinesq approximation to describe the motion of a viscous and incompressible fluid (see e.g. Jones, 2011). Gravity $\vec{g}$ and the initial density stratification $\rho_0(r)$ of the core fluid are both radial, so the buoyancy force has only a radial component $-(\rho g\hat{r})$, where ρ is the fluid density at any subsequent time (see Eq. 6). The centrifugal force that arises in the rotating frame is incorporated in the pressure term ∇P, but the magnetic force is expressed in terms of the Maxwell magnetic stress tensor T without absorbing the magnetic pressure into P:

$$T_{ij} = \left(B_i B_j - \frac{1}{2}B^2\delta_{ij}\right). \tag{1}$$

With these simplifications, the momentum equation becomes

$$\rho\frac{D\vec{V}}{Dt} = -\nabla P + \frac{1}{\mu_0}\nabla\cdot T + \rho\nu\nabla^2\vec{V} - 2\rho\Omega\times\vec{V} - \rho g\hat{r}. \tag{2}$$

As we retain pressure as a variable, we must explicitly enforce the continuity equation

$$\nabla\cdot\vec{V} = 0. \tag{3}$$

We use the magnetohydrodynamic approximation (e.g. Roberts and King, 2013) to describe the evolution of the magnetic field

$$\frac{\partial\overrightarrow{B}}{\partial t} = \nabla\times(\vec{V}\times\overrightarrow{B}) + \eta\nabla^2\overrightarrow{B} \tag{4}$$

where $\eta = 1/(\sigma\mu_0)$ is the magnetic diffusivity. The magnetic field is also subject to the condition

$$\nabla\cdot\overrightarrow{B} = 0. \tag{5}$$

2.2. Thin-layer approximation

The governing equations are linearized by assuming that the waves are small perturbations of a background state

$$\vec{V} = \vec{V_0} + \vec{v}, \quad U_r = U_{r0} + u_r, \quad \overrightarrow{B} = \overrightarrow{B_0} + \vec{b}, \quad P = P_0 + p, \quad \rho = \rho_0 + \Delta\rho \tag{6}$$

In a thin layer, radial velocities are relatively small, so the radial force balance is nearly hydrostatic. We also adopt a hydrostatic background state

$$\vec{V_0} = 0, \quad U_{r0} = 0 \tag{7}$$

where P_0 and ρ_0 are the hydrostatic pressure and initial density profile.

For the radial buoyancy force, the local density of the fluid ρ is disturbed by radial motion through the (radial) background density gradient $\partial\rho_0/\partial r$. Assuming the displacement of the parcel (u_r) is small,

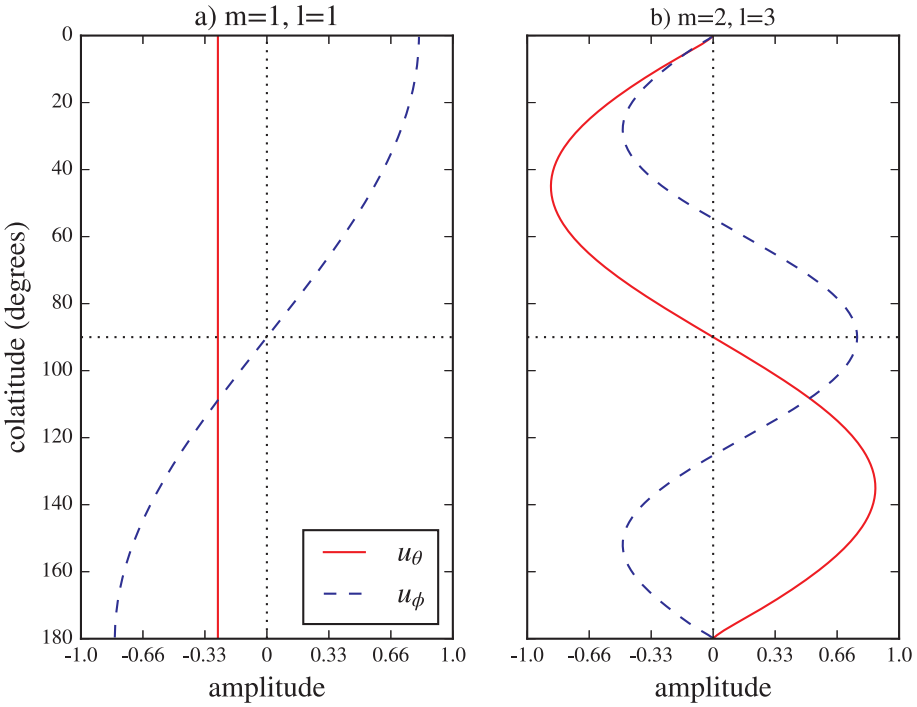

Fig. 2. Longitudinal slices of velocity fields for Rossby wave modes with peak velocity normalized to 1. (a) $\ell = 1, m = 1$ and (b) $\ell = 3, m = 2$. Note that (a) includes non-zero flow at the poles – no modifications to the method are required to handle this case.

the density perturbation can be written as $\Delta\rho = -u_r \partial\rho_0/\partial r$. The buoyancy force can therefore be written

$$-\rho g\,\hat{r} = -(\rho_0 g - \rho_0 \frac{g}{\rho_0}\frac{\partial \rho_0}{\partial r} u_r)\hat{r} = -(\rho_0 g + \rho_0 N^2 u_r)\hat{r} \tag{8}$$

where

$$N = \sqrt{-\frac{g}{\rho_0}\frac{\partial \rho_0}{\partial r}} \tag{9}$$

is the Brünt-Vaïsaïlla frequency, which defines the strength of stratification. In this model, we allow both N and B_0 to vary with radius r and colatitude θ through the layer

$$N = N(r,\theta), \qquad \vec{B_0} = \vec{B_0}(r,\theta)$$

The radial component of the momentum Eq. (2) is nearly hydrostatic, so the radial gradient in the pressure perturbation balances the buoyancy force

$$0 = -(\nabla p)_r - N^2 u_r \tag{10}$$

where the subscript r is used to denote the radial component of a vector quantity.

Pressure perturbations induced by radial motion drive a horizontal flow. We make the usual assumption of retaining only the radial component of the rotation vector in the governing equations (i.e. $\Omega_r = \Omega\cos\theta$) because the horizontal component contributes to the Coriolis force only through the (small) radial velocity. Therefore, subtracting the hydrostatic state (7) and eliminating small terms, the horizontal momentum Eqs. (2) become

$$\frac{\partial \vec{v}_{\theta,\phi}}{\partial t} = -\frac{1}{\rho_0}(\nabla p)_{\theta,\phi} + \frac{1}{\rho_0 \mu_0}(\nabla \cdot T_l)_{\theta,\phi} + \nu(\nabla^2 \vec{v})_{\theta,\phi} - 2(\Omega cos\theta\,\hat{r}) \times \vec{v} \tag{11}$$

where T_l is a linearized version of the Maxwell stress tensor T retaining only terms involving interactions between B_0 and b. Note that we retain the viscous force to promote numerical stability, although this term is typically quite small.

Small radial velocities relative to horizontal velocities ($v_r \ll v_{\theta,\phi}$) are expected when the characteristic radial length scale is small compared with the horizontal length scale. The corresponding radial magnetic perturbations are also very small ($b_r \ll b_{\theta,\phi}$) as they are related through the induction Eq. (4). Consequently, we solve for the horizontal perturbations in the magnetic field using the induction equation

$$\frac{\partial b_{\theta,\phi}}{\partial t} = (\nabla \times \vec{v} \times \vec{B_0})_{\theta,\phi} + (\eta \nabla^2 \vec{b})_{\theta,\phi} \tag{12}$$

and evaluate the radial component (if needed) using the solenoidal condition $\nabla \cdot \vec{b} = 0$.

2.3. Non-dimensionalization

The equations are cast into a non-dimensional form using the core radius R_c as the characteristic lengthscale and the reciprocal rotation rate of the earth $1/\Omega$ for the characteristic time scale (see Table 1). This results in two dimensionless constants – the Ekman number E and the magnetic Prandtl number P_m – and two dimensionless parameters that can vary through the layer – buoyancy frequency N_Ω and a dimensionless radial magnetic field B_r (see Table 2). Here, the characteristic magnetic field $B' = \sqrt{\rho\eta\mu_0\Omega}$ is 0.86 mT for $\eta = 0.8\,\mathrm{m}^2/\mathrm{s}$, but can vary with different choices for core conductivities. Collecting terms, the governing Eqs. (11) and (12) become

$$\frac{\partial v_{\theta,\phi}}{\partial t} = -\nabla p + \frac{E}{P_m}(\nabla \cdot T_l)_{\theta,\phi} + E\nabla^2 \vec{v} - 2(\cos\theta \hat{r}) \times \vec{v} - N_\Omega^2 u_r \hat{r} \tag{13}$$

and

Table 1
Physical constants used for model.

Symbol	Constant	Value
Ω	Rotation Rate of Earth	7.3×10^{-5}/s
R_c	Radius of Outer Core	3480 km
ν	Momentum Diffusivity	10^{-2} m^2/s
η	Magnetic Diffusivity	0.8 m^2/s
ρ_0	Density	10^4 kg/m^3
μ_0	Vacuum Permeability	1.26×10^{-6} m kg/s^{2}A^2
N	Brunt-Väisälä Frequency	$O(1\Omega)$

Table 2
Non-dimensional parameters with representative values.

Parameter	Definition	Value in Core	Value in Model
E	$\frac{\nu}{R_c^2\Omega}$	$10^{-15} - 10^{-14}$	10^{-11}
P_m	$\frac{\nu}{\eta}$	$10^{-6} - 10^{-5}$	10^{-2}
N_Ω	$\frac{1}{\Omega}\sqrt{\frac{-g}{\rho_0}\frac{\partial \rho_0}{\partial r}}$	$0-10^1$	$0-10^1$
B_r	$\vec{B_0}\cdot\hat{r}/\sqrt{\rho\eta\mu_0\Omega}$	0.1 – 1.0	0.0 – 1.0

$$\frac{\partial b_{\theta,\phi}}{\partial t} = (\nabla \times \vec{v} \times B_r)_{\theta,\phi} + \frac{E}{P_m}(\nabla^2 \vec{b})_{\theta,\phi} \tag{14}$$

where variables now represent their non-dimensional forms. The equations are supplemented by the incompressibility condition

$$\nabla\cdot\vec{v} = 0 \tag{15}$$

and a linearized relationship between u_r and v_r

$$\frac{\partial u_r}{\partial t} = v_r. \tag{16}$$

2.4. Hybrid finite volume – fourier method

The governing equations are discretized using a combination of finite volume (e.g. Ferziger and Peric, 2002) and Fourier methods, jointly abbreviated as FVF. The domain is split into cells with a regular spacing in radius and colatitude. Each term in the governing equations is integrated over the cell volume then converted into a surface integral using Gauss' theorem. We then divide this quantity by the cell volume to obtain an operators that look similar to those used in finite difference methods. Each cell is indexed by the letter k in the radial direction and l in the latitudinal direction, while the letter m denotes the longitudinal wave number of the Fourier mode. Radial positions r,r_+, and r_-, respectively, denote the location of the center, top, and bottom faces of the cell in question, and Δr denotes the radial thickness of the cell. An analogous notation is used for the meridional position (i.e. θ,θ_+,θ_-). An example of a cell is shown in Fig. 1. We demonstrate the approach by deriving the (discrete) operator for the radial pressure gradient.

For the radial pressure gradient,

$$(\nabla p)_r = \left(\frac{1}{\Delta V}\int_S p\, \overrightarrow{dS}\right)\cdot\hat{r} \tag{17}$$

where $\Delta V = r^2\sin\theta\Delta r\Delta\theta\Delta\phi$ represents the volume of the cell and the integral is taken over the total surface S (e.g. Aris, 1962). The surface integral is subdivided into individual faces, where A_{r_+} and A_{r_-} denote the area of the top and bottom radial faces and $\hat{n}_{r_+}$ and $\hat{n}_{r_-}$ represent the vectors normal to those faces (see Fig. 1). A similar notation is used for the other faces. Summing the contributions from all six faces gives

$$\begin{aligned}(\nabla p)_r = \frac{1}{\Delta V}\{&p_{r_+}A_{r_+}(\hat{r}\cdot\hat{n}_{r_+}) + p_{r_-}A_{r_-}(\hat{r}\cdot\hat{n}_{r_-}) + p_{\theta_+}A_{\theta_+}(\hat{r}\cdot\hat{n}_{\theta_+})\\ &+ p_{\theta_-}A_{\theta_-}(\hat{r}\cdot\hat{n}_{\theta_-}) + p_{\phi_+}A_{\phi_+}(\hat{r}\cdot\hat{n}_{\phi_+}) + p_{\phi_-}A_{\phi_-}(\hat{r}\cdot\hat{n}_{\phi_-})\}.\end{aligned} \tag{18}$$

Interpolating the surface values of p using the values at the centers of adjacent cells, we obtain

$$\begin{aligned}(\nabla p)_r^{(k,l)} = &\frac{r_+^2}{2r^2\Delta r}p^{(k+1,l)} - \frac{r_-^2}{2r^2\Delta r}p^{(k-1,l)} - \frac{\sin\theta_+}{4r\sin\theta}p^{(k,l+1)} - \frac{\sin\theta_-}{4r\sin\theta}p^{(k,l-1)}\\ &- \frac{\sin\theta_+ + \sin\theta_-}{4r\sin\theta}p^{(k,l)}.\end{aligned} \tag{19}$$

This expression appears similar to a finite difference operator, but correctly accounts for the spherical geometry of the domain and does not introduce coordinate singularities at the north and south poles. The $\hat{\theta}$ component of the pressure gradient is derived in a similar manner and results in a similar expression. The $\hat{\phi}$ component is somewhat simpler because we use the Fourier series to interpolate values onto the ϕ-faces of the cell. Adopting the small angle approximation $\sin\Delta\phi/2 \approx \Delta\phi/2$, the expression for $(\nabla p)_\phi$ simplifies into

$$(\nabla p)_\phi^{(k,l)} = \left(\frac{im}{r\sin\theta}\right)p^{(k,l)} \tag{20}$$

where m represents the Fourier mode.

Expressions for all other terms in the governing equations are derived in a similar manner. We introduce short-hand notation for the derived numerical operators to simplify notation. For example, the divergence operator can be represented as

$$\nabla\cdot\vec{v} = \nabla_r v_r + \nabla_\theta v_\theta + \nabla_\phi v_\phi \tag{21}$$

where ∇_r,∇_θ,∇_ϕ represent numerical operators that include terms due to the spherical geometry of the problem (e.g. $\nabla_r \neq \partial_r$). Details of these derivations and the resulting operators can be found in the supplement.

2.5. Eigenvalue formulation

Perturbations in the fields are constrained to vary periodically in time and longitude with complex time frequency ω and longitudinal wavenumber m:

$$\begin{bmatrix}\vec{v}(r,\theta,\phi,t)\\ b_{\theta,\phi}(r,\theta,\phi,t)\\ p(r,\theta,\phi,t)\\ u_r(r,\theta,\phi,t)\end{bmatrix} = \begin{bmatrix}\vec{v}(r,\theta)\\ b_{\theta,\phi}(r,\theta)\\ p(r,\theta)\\ u_r(r,\theta)\end{bmatrix} e^{i(\omega t + m\phi)}. \tag{22}$$

Applying this constraint and introducing the notation from Section 2.4, the final governing equations for the model are

$$0 = -(\nabla p)_r - N_\Omega^2 u_r \tag{23a}$$

$$i\omega v_\theta = -(\nabla p)_\theta + \frac{E}{P_m}(\nabla\cdot T_l)_\theta + E(\nabla^2\vec{v})_\theta + 2\cos\theta\, v_\phi \tag{23b}$$

$$i\omega v_\phi = -(\nabla p)_\phi + \frac{E}{P_m}(\nabla\cdot T_l)_\phi + E(\nabla^2\vec{v})_\phi - 2\cos\theta\, v_\theta \tag{23c}$$

$$i\omega b_\theta = (\nabla\times\vec{v}\times B_r\hat{r})_\theta + \frac{E}{P_m}(\nabla^2\vec{b})_\theta \tag{23d}$$

$$i\omega b_\phi = (\nabla\times\vec{v}\times B_r\hat{r})_\phi + \frac{E}{P_m}(\nabla^2\vec{b})_\phi \tag{23e}$$

$$0 = \nabla_r v_r + \nabla_\theta v_\theta + \nabla_\phi v_\phi \tag{23f}$$

$$i\omega u_r = v_r. \tag{23g}$$

Note that we do not explicitly solve for b_r because its effect on the dynamics is very small. However, the magnetic induction Eqs. (23d) and (23e) in combination with mass continuity (23f) enforce the condition $\nabla\cdot\vec{b} = 0$ when the initial field is solenoidal, and b_r can always be recovered from the solution using the solenoidal condition.

2.6. Boundary conditions

Boundary conditions are needed at the top and bottom radial surfaces of the layer to close the equations. However, we do not need conditions at $\theta = 0$ and $\theta = \pi$ in the FVF method because the area of the face of the cell adjoining the north and south pole vanishes and thus does not contribute to the surface integral.

At the CMB we impose no radial motion and adopt (viscous) stress-free boundary conditions because viscous boundary layers are not expected to play a large role in the dynamics of the waves when the Ekman number (E) is small. Consequently, the boundary conditions on velocity at the CMB are

$$v_r = 0, \qquad \frac{\partial v_\theta}{\partial r} = 0, \qquad \frac{\partial v_\phi}{\partial r} = 0. \tag{24}$$

The conditions at the bottom boundary of the layer are more complex. Viscous stress-free conditions are reasonable when E is small, but it is not obvious that the radial motion should vanish. Numerical calculations show that the radial motion is indeed small for zonal MAC waves when the underlying region is geostrophic (Buffett, 2014). Braginsky also argued for no radial motion at the bottom boundary for non-zonal waves by introducing a density jump at the base of the layer (Braginsky, 1998). When the density jump is large enough the associated buoyancy suppresses radial motion at the boundary. Gravity waves can propagate along the interface, but the periods are short compared with the period of non-zonal MAC waves, so the motion is effectively decoupled. As long as the timescale of dynamics in the interior is different enough from the period of waves in the layer, then it seems reasonable to decouple the motion in these two regions. We do this by adopting (24) as boundary conditions on the base of the layer.

These conditions are incorporated directly into FVF discretization for cells adjoining the top and bottom boundaries, with details found in the supplement.

The appropriate conditions on pressure follow directly from (23a). When either the radial motion or the stratification (N) vanishes, we require

$$\frac{\partial p}{\partial r} = 0 \tag{25}$$

at the top and bottom boundary of the layer. These are again implemented directly into the FVF operators, with details in the supplement.

A natural choice of boundary conditions for the magnetic field at the CMB is to match the numerical solution to a potential field outside the core. These boundary conditions are not easily implemented in a finite volume formulation, but fortunately the pseudo-vacuum boundary conditions

$$b_{\phi,\theta}|_{CMB} = 0 \tag{26}$$

are a good approximation. Braginsky (1998) offers a detailed discussion of these boundary conditions for waves in a thin layer, but they can be justified with a simple physical argument. In the mantle, horizontal and radial components of a potential magnetic field perturbation are of the same order $b_{\theta,\phi}|_{\text{mantle}} \sim b_r|_{\text{mantle}}$. However, in a thin layer, horizontal perturbations to the magnetic field are much larger than the radial perturbations due to large horizontal fluid motions, $b_{\theta,\phi}|_{\text{layer}} \gg b_r|_{\text{layer}}$. The magnetic field must be continuous, so at the CMB, $b_{\theta,\phi}$ must be similar in magnitude to b_r. Thus, $b_r|_{\text{CMB}} \sim b_{\theta,\phi}|_{\text{CMB}} \ll b_{\theta,\phi}|_{\text{layer}}$. As the horizontal perturbation of the magnetic field is much smaller at the CMB than within the layer, we can adopt the conditions shown in (26) without significantly affecting the wave dynamics.

At the bottom of the layer, the boundary conditions for the magnetic field must match the solution for a perturbation in the conductive fluid deeper inside the core. The waves we wish to study require buoyant stratification to propagate and thus decay in the region below where there is no buoyant restoring force. However, these waves do interact with the convective fluid in the bulk of the core through magnetic induction and pressure and potentially couple to modes of oscillations in the bulk of the core. To fully treat this problem would require a description of motion through the whole core, which is beyond the scope of this work. Instead, we choose to simulate only the stratified layer region and approximate the bulk of the core fluid as stationary, allowing the magnetic perturbation to propagate into the core with a skin depth dependent on the period of oscillation.

To implement this boundary condition in our model, we require the magnetic field to be continuous across the bottom boundary and integrate the induction equation across the interface, assuming that horizontal gradients in the magnetic field are negligible compared to radial gradients. The continuity condition becomes

$$B_r [v_{\theta,\phi}]^+_- + \frac{E}{P_m}[\partial_r b_{\theta,\phi}]^+_- = 0 \tag{27}$$

where $[\,]^+_-$ denotes the discontinuity in quantities above (+) and below (−) the bottom layer boundary. The velocity above the boundary does not vanish because we impose viscous stress free conditions. Below the boundary, $v^-_{\theta,\phi} = 0$ and the magnetic perturbation inside the core obeys a diffusion equation. The solution below the layer is

$$b^-_{\theta,\phi}(r - r_b) = b^+_{\theta,\phi}(r_b) e^{[(1+i)(r-r_b)/\delta]} e^{i(\omega t + m\phi)} \tag{28}$$

where r_b denotes the radial location of the bottom layer boundary and δ denotes the dimensionless magnetic skin depth

$$\delta = \sqrt{\frac{2E}{\omega P_m}}. \tag{29}$$

Using (28) to evaluate the boundary condition in (27) gives

$$B_r v^+_{\theta,\phi} + \frac{E}{P_m}\partial_r b^+_{\theta,\phi} - \frac{(1+i)}{\delta} b^+_{\theta,\phi} = 0. \tag{30}$$

When the magnetic perturbation at $r = r_b$ is mainly due to the velocity discontinuity at the base of the layer, it is reasonable to approximate $\partial_r b^+_{\theta,\phi}$ using the diffusive solution complementary to (28). In this case, the boundary condition reduces to

$$b^+_{\theta,\phi} = \frac{\delta B_{0r} P_m}{2(1+i)E} v^+_{\theta,\phi} \tag{31}$$

with further details found in the supplement.

As the magnetic skin depth depends upon the period of the wave, these boundary conditions require knowledge of the period of the waves prior to solving the eigenvalue problem. Thus, we use an iterative approach: an estimate of the wave period is used for the initial calculation, then the solution is recomputed using the updated wave period. Typically, convergence requires only a few iterations.

2.7. Solving the eigenvalue problem

Incorporating boundary conditions into the discrete operators, the governing Eqs. (23) are cast into the form of a generalized eigenvalue problem $\omega \mathbf{B}\mathbf{x} = \mathbf{A}\mathbf{x}$ where $\mathbf{A}$ and $\mathbf{B}$ are sparse matrices, ω is the eigenvalue, and $\mathbf{x}$ is the eigenvector containing the wave structure for each variable. We let

$$\mathbf{x}^T = [v_r, v_\theta, v_\phi, b_\theta, b_\phi, p, u_r]. \tag{32}$$

where each variable is indexed first by cell radial coordinate k, then cell latitudinal coordinate l. In other words, the first two elements of v_r are $v_r(k = 0, l = 0)$ and $v_r(k = 1, l = 0)$. Thus, $\mathbf{x}$ is a vector with $7 \times N_r \times N_\theta$ components, where N_r and N_θ are the number of radial and latitudinal cells in the model, respectively. With this formulation, $\mathbf{B}$ is a singular semi-positive definite mass matrix consisting only of ones and zeros on the diagonal representing time derivatives and $\mathbf{A}$ is a sparse block matrix containing the rest of equation dynamics and boundary conditions.

Typical model runs have $N_r \sim 40$ and $N_\theta \sim 200$, so that $\mathbf{x}$ has $\sim$ 56,000 components. The matrices are extremely sparse; most submatricies only require storing a few terms near the diagonal. Although $\mathbf{A}$ is a $(7N_rN_\theta \times 7N_rN_\theta)$ matrix with $(7N_rN_\theta)^2 \sim O(10^9)$ possible components, it only requires the storage of $O(100 \times 7N_rN_\theta) \sim O(10^6)$ terms due to the sparsity of the discretized FVF operators.

Matrices are assembled in the Python language using the sparse matrix toolkits included in the scipy and numpy packages (Van Der Walt et al., 2011; Jones et al., 2001). After the matrices are assembled in Python, the eigenproblem is solved using the Scalable Library for Eigenvalue Problem Computations (SLEPc) (Hernandez et al., 2005). A desired wave frequency ω_0 is targeted using the shift–invert technique. The shifted eigenproblem is then solved using an iterative Krylov–Schur

method, finding the requested number of solutions with frequencies closest to the desired wave frequency ω_0. The Krylov–Schur method normalizes the eigenvector each iteration, minimizing the pressure term and removing its extra degree of freedom (recall that the boundary conditions on p leaves the average amplitude unconstrained). The eigenvector contains information about the structure of the wave, and the eigenvalue specifies the wave period and decay rate. Since the eigenvector is unconstrained up to a constant factor, the amplitude of the wave is determined by defining an excitation or by comparison to observed secular variation and inferred core fluid velocities.

3. Results

Using the FVF method, we are able to examine the effect of different magnetic field configurations on magnetohydrodynamic waves in Earth's core. We first verify the technique by deriving global waves with a reduced subset of the equations. We choose global barotropic Rossby waves because they have an exact analytical solution to compare against and they demonstrate that our formulation allows flow directly across the north and south poles. Next, we examine the effect of non-dipolar fields on the structure of zonal MAC waves and compare to the results of Braginsky (1993) and Buffett (2014). Finally, we study the effects of varying magnetic field strength and structures on the spatial extent and characteristics of non-zonal MAC waves, with relevance to recent observations by Chulliat et al. (2015).

3.1. Global barotropic rossby waves

Barotropic Rossby waves arise in a thin spherical shell of fluid due to interactions between inertia, pressure, and the Coriolis force:

$$\frac{\partial \vec{v}}{\partial t} = -\frac{1}{\rho}\nabla p - 2\Omega \times \vec{v} \tag{33}$$

Solutions for Rossby waves are well studied (e.g. Platzman, 1968) and can be expressed in terms of a streamfunction formulation for the velocity field

$$\vec{v} = \nabla \times \Psi \hat{r}. \tag{34}$$

The radial component of the curl of the governing Eq. (33) can be written in terms of the streamfunction as

$$\frac{\partial \nabla^2 \Psi}{\partial t} = -\frac{2\Omega}{r^2}\partial_\phi \Psi \tag{35}$$

which for vertically invariant fluid motions admits solutions of

$$\Psi = C P_\ell^m(\cos\theta) e^{i(m\phi + \omega t)} \tag{36}$$

where $P_\ell^m(x)$ are the associated Legendre polynomials and C is an arbitrary constant. Note that degree ℓ is distinct from index l, which is used previously to denote latitudinal grid cell in the FVF method. Substituting (36) into (35) gives an expression for the wave frequency

$$\omega_{\text{Rossby}} = \frac{2m}{\ell(\ell+1)}\Omega. \tag{37}$$

Rossby waves emerge from our numerical model by removing the influence of magnetic field and fluid stratification. Fig. 2 shows numerical solutions for two wave modes: one specified by $\ell = 1, m = 1$ and the other by $\ell = 3, m = 2$. Numerical and analytical solutions were found to agree precisely with a grid size of 20 radial and 120 latitudinal cells, with a maximum root mean squared error between normalized velocity fields of 1.6×10^{-4} and wave periods in agreement to four significant digits. Note that the FVF model correctly computes the Rossby wave with $\ell = 1, m = 1$ which represents a solid-body rotation around an equatorial axis and includes flow across the north and south poles.

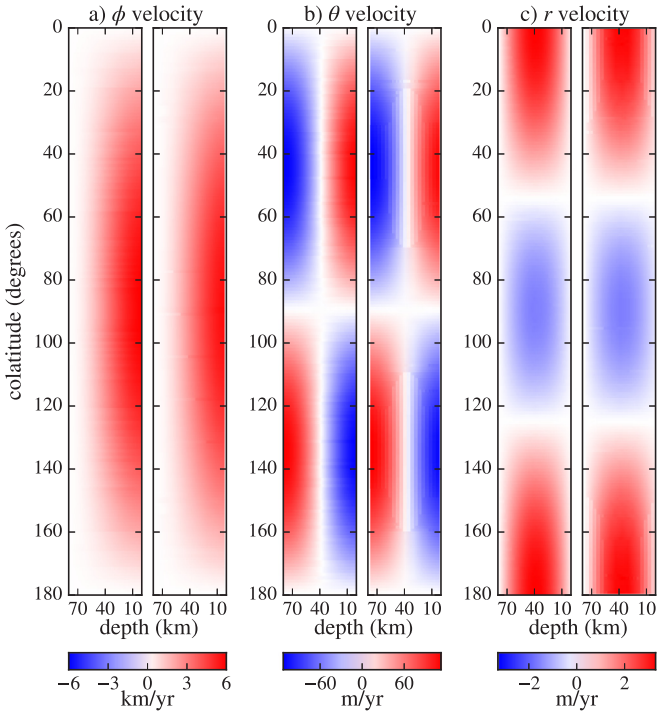

Fig. 3. Comparison of Braginsky analytical (left) and FVF numerical (right) solutions for zonal MAC waves with Braginksy's preferred parameters H = 80 km, N = 2Ω,η = 2 m^2/s,B_d = 0.5 mT. Longitudinal (a), latitudinal (b), and radial (c) components of flow are shown for a meridional slice through the stable layer, with (a) offset 90° in phase. The relative amplitudes of the flow are fixed in the solution, but the overall magnitude is unconstrained. A representative estimate for v_ϕ is chosen for comparison to waves in Earth's core.

3.2. Zonal magnetic archimedes coriolis (MAC) waves

Analytical solutions for zonal MAC waves were given by Braginsky (1993). He adopted a constant buoyancy frequency through the layer and used the radial component of a dipole as the background magnetic field. He proposed the same boundary conditions as those assumed in our FVF model, although he relaxes the bottom boundary conditions to pseudo-vacuum conditions to derive the leading-order analytical solution. His lowest frequency wave (at latitudinal degree $\ell = 2$) is compared with the results of our FVF model in Fig. 3. Wave structures are nearly identical, with very small (<2%) differences in the relative amplitudes of the flow components. Braginsky's expression for the wave period gives 63.42 years with his preferred layer parameters (see Fig. 3 caption), while the FVF model gives 72.8 years. Most of this discrepancy arises because Braginsky discards diffusion when deriving his expression for the wave period. When we reduce the magnetic diffusivity in our model by a factor of four the wave period becomes 63.34 years, a difference of only ~ 0.1%.

Our FVF model is also able to reproduce numerical MAC wave results from a previous spectral model (Buffett, 2014). The two lowest-order MAC waves for the case of constant buoyancy and constant radial magnetic field were compared for two different values of N_Ω. Wave structures and periods converged to a stable solution with a resolution of 20 radial by 120 latitudinal cells, with rms error of the wave structures within 1% and wave periods and quality factors ($Q = \Re(\omega)/2\Im(\omega)$) within 2% for both modes.

Unlike the analytical or spectral decomposition solutions, the FVF model permits the study of more general background magnetic field configurations than just constant or dipole fields. Earth's observed field is neither constant nor a perfect dipole, but instead has a dominant dipole structure with a significant amount of higher-order structure overlaid. As the Lorentz force takes the form $\vec{B}\cdot\nabla(\vec{B})$ in the

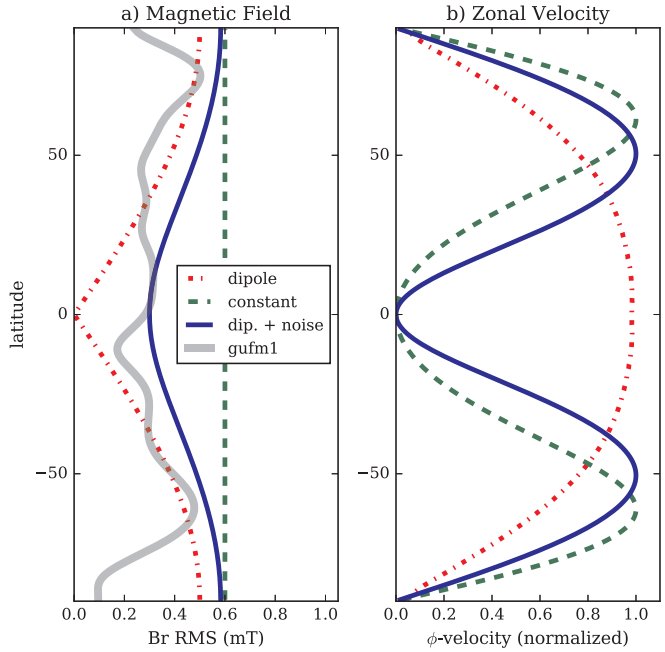

Fig. 4. Comparison of MAC wave zonal flow velocities (v_ϕ) for three choices of radial magnetic field. We include a dipole field (Braginsky, 1993), a constant field, and a dipole plus noise (see text), which is intended to approximate gufm1 at 1990 (Jackson et al., 2000). All runs use H = 80 km, N = 2Ω. Note that a finite magnetic field strength at the equator causes v_ϕ to vanish.

magnetohydrodynamic approximation, it is insensitive to the polarity of the field. Then, as waves in a thin layer are mainly sensitive to the radial magnetic field, it is appropriate to examine the root-mean-square (RMS) radial magnetic field strength as a function of latitude. It can be seen in Fig. 4a that historical observations of the average magnetic field strength by latitude at the CMB show a RMS field strength of ~0.5 mT at high latitudes and ~0.3 mT near the equator (Jackson et al., 2000). This represents a lower bound on the total field at the CMB, as unobserved small-scale features likely contribute to the total RMS field at the CMB. To approximate the structure of the total field at the CMB, we add white noise to a dipole field and take the root-mean-square of the distribution, giving

$$B_r^{rms}(\theta) = \sqrt{B_d^2 \cos^2\theta + \sigma^2}. \tag{38}$$

Values of $B_d = 0.5$ mT and $\sigma = 0.3$ mT are chosen to approximate Earth's observed CMB field with a small amount of unobserved noise (Fig. 4a). Braginsky (1998) used the same value for his dipole but did not include noise, resulting in zero field strength at the equator. The core's internal radial magnetic field is also likely to vary with radius. While our model can accommodate radial variations, the details of these variations are unknown and likely to be small in a thin layer, so these preliminary results simply use the CMB field throughout the layer depth.

The dipole with noise approximation of the total field produces MAC waves with peak zonal flows at mid-latitudes and no flow at the equator, in stark contrast to MAC waves derived using a dipole, which have peak flow on the equator. A dipole permits flow at the equator because the force balance between the Lorentz and Coriolis forces are perfectly maintained as they become weaker near the equator. However, non-zero field strength at the equator alters the force balance in the ϕ-component of the momentum equation. To a first approximation, we have a balance between the Coriolis force $2\Omega\cos\theta\, u_\theta$ and the Lorentz force $B_r \partial_r b_\phi$. When B_r is dipolar, we can achieve a balance between the Coriolis and Lorentz forces with a non-zero $\partial_r b_\phi$ at the equator. Otherwise, if B_r is finite at the equator, $\partial_r b_\phi$ must vanish at the equator to maintain the force balance, which precludes any source of generation due to u_ϕ. Consequently, u_ϕ must be zero at the equator for these wave motions.

This result demonstrates the importance of magnetic field configurations when studying waves in Earth's core. Braginsky's MAC wave solution is only valid due to the precise balance between Coriolis and Lorentz forces near the equator resulting from a perfect dipole field, and even small perturbations to B_r alter the basic structure of the solution significantly. Because Earth's field includes significant power near the equator, a constant radial field seems to be a better approximation than a dipole field for MAC waves, as it produces a similar basic wave structure. However, both the dipole and constant field approximations give very different wave structures and properties to those derived using a more realistic magnetic field configuration with our FVF method.

3.3. Non-zonal MAC waves

Strong equatorial flux patches with varying intensity are observed in many core-surface magnetic field models (e.g. Finlay et al., 2016). Chulliat examines these patches using measurements of magnetic secular acceleration and finds oscillating signals consistent with waves travelling both east and west with periods between six and ten years (Chulliat et al., 2015). He appeals to waves propagating in a stratified layer to explain these observations and cites a prior study by Bergman (1993). However, approximations Bergman uses in his derivation of analytical solutions lead to purely damped perturbations (see eq. 3.6 in that study). Bergman also performs numerical computations (Figs. 2 and 3 in that study), but only finds propagating waves with periods of several months or less, and these solutions required unrealistically strong stratification and weak magnetic fields. Therefore, it is reasonable to question the use of this model to interpret longer period motions in magnetic secular acceleration. Indeed, Bergman recognizes this when he states "…we do not know the relevance of the solutions to the H layer" (Bergman, 1993). We use our model to determine whether equatorially trapped waves with properties similar to Chulliat's observations can arise with physically plausible magnetic field configurations and stratified layer properties.

We examine waves with a zonal wavenumber of m = 6 to correspond to the strongest signal observed in recent secular accelerations. In our initial investigations, we computed non-zonal MAC waves in a 140 km thick layer with N=Ω and found periods of hundreds to thousands of years, more than an order of magnitude larger than observations. Closer agreement between our equatorial waves and observed wave periods requires thinner layers with stronger stratification. Based on previous estimates for properties of a layer arising from compositional stratification, we examine waves in a layer that is 20 km thick with a constant buoyancy of N = 10 Ω (Gubbins and Davies, 2013; Buffett and Seagle, 2010) and are able to find equatorial waves propagating to the east with periods roughly matching observations for reasonable (~0.5 mT) magnetic field strength. We are also able to find westward propagating waves, but they require very strong (~10 mT) radial magnetic fields to match the short periods observed, which may cast some doubt on this explanation for the observations.

On the other hand, the existence of a thin, strongly stratified layer is very plausible. For example, barodiffusion would produce a layer of strong stratification (Gubbins and Davies, 2013), particularly in a broader region of stable thermal stratification. In fact, it is difficult to prevent a compositionally stratified layer from forming. Numerical calculations show that a thin layer of compositional stratification inside a thicker layer of thermal stratification would not substantially alter the period of low-frequency zonal MAC waves in the thicker layer, although it could lower the amplitude of flows at the CMB depending on the thickness of the stronger sub-layer.

One intriguing feature of these equatorially-trapped non-zonal MAC waves is their dependence on the background magnetic field. The frequency of the waves depends mainly on the RMS strength of the

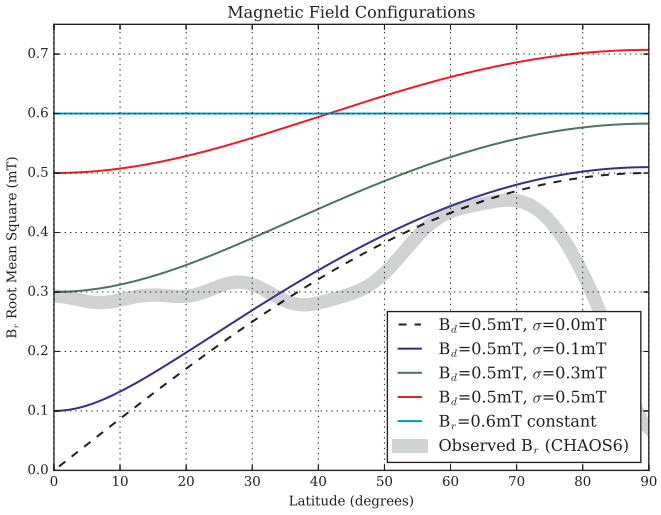

Fig. 5. Magnetic field distributions used for non-zonal MAC wave solutions in Fig. 6. Note that small noise values have relatively high (low) field strength at high (low) latitudes, while large noise values results in field structures more evenly distributed across latitude. Included for comparison is the observed zonal-averaged RMS radial core field in 2010 from the CHAOS-6 field model (Finlay et al., 2016).

background field, with stronger fields producing shorter periods. However, the spatial structure of the waves is largely insensitive to changes in the total RMS field. Instead, the spatial distribution of background magnetic field has a large influence on the latitudinal extent of the waves. We compute several wave solutions using (38) to construct a range of simple models for the radial magnetic field, including a dipole with several different amounts of noise and a constant radial field (see Fig. 5). A nearly dipolar field with only 0.1mT noise produces strong equatorial trapping, with peak flow near the equator (see Fig. 6). Larger amounts of noise result in stronger relative field strengths in the equatorial region and produce waves that are less confined to the equator. In the limit of a constant radial field the peak flow velocities occur at mid-latitudes. Because the spatial distribution of magnetic field strength is important in determining the spatial structure of the waves, the spatial extent of oscillations in observed secular acceleration could provide a constraint on distribution of total magnetic field strength at the CMB, including small scale structures unable to be observed directly.

Further examination of these waves is needed before drawing strong conclusions, as there are many differences between our computed waves and Chulliat's observations. First, the equatorial waves we find propagate only to the east with reasonable magnetic field strengths, unlike Chulliat's observed waves which propagate in both directions. In addition, some of the sub-decadal waves found are heavily damped. Some waves have quality factors ($Q = \Re(\omega)/2\Im(\omega)$) less than one, whereas others have much higher quality. Finally, we need to further explore how a thin, strongly-stratified layer overlying a thicker layer of weak stratification would impact the zonal MAC waves studied in (Buffett, 2014). Further examination of layer and magnetic field structures are needed to see if there exist waves and layer structures that can explain all observed signals.

4. Conclusions

We have developed a new hybrid finite volume and Fourier (FVF) numerical model to study magnetohydrodynamic waves in a thin stratified layer in Earth's core. The FVF model is flexible and extensible, allowing for spatially varying buoyancy and background magnetic fields in both depth and latitude. We have validated it by comparison to previous analytical and numerical results and have shown that waves derived using simple background fields have very different structures than those derived with more realistic fields.

With additional high-resolution observations of the geomagnetic field constantly being collected, techniques to study core dynamics and properties utilizing observations of GSV will become increasingly useful. We have shown that interpreting observed periodic signals requires an accurate treatment of the latitudinal configuration of the background magnetic field when deriving wave modes, which is now

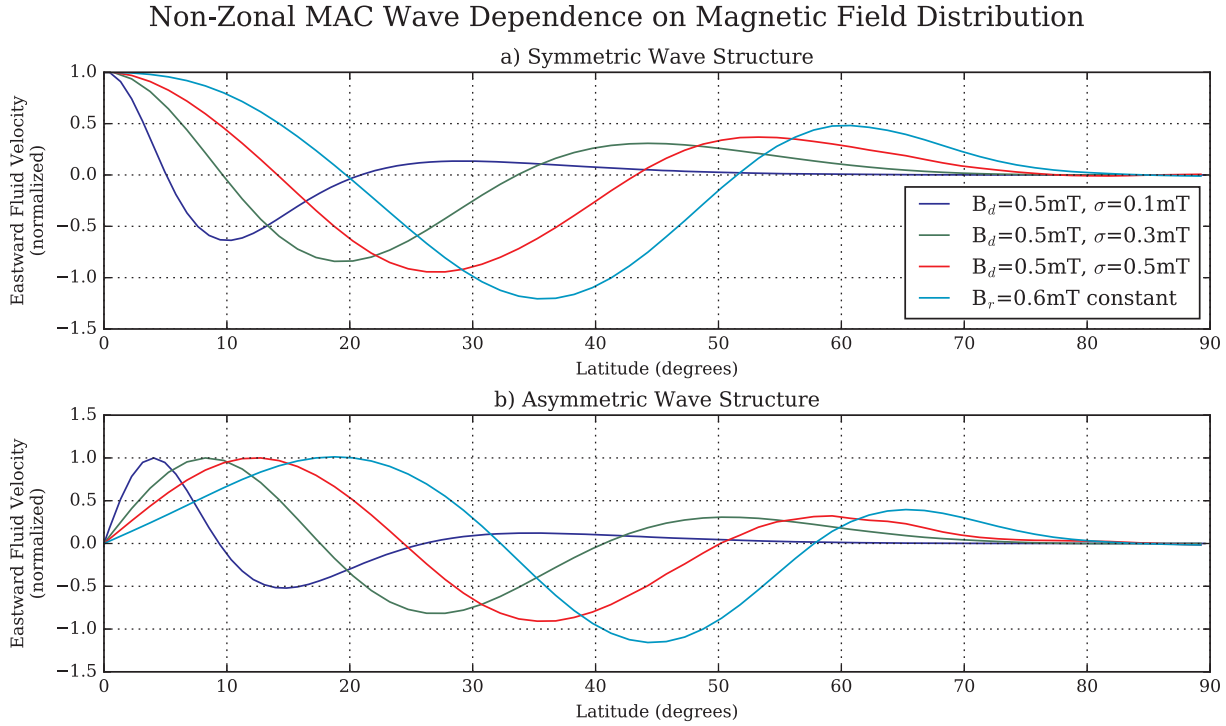

Fig. 6. Comparison of wave structures of four non-zonal MAC waves computed using four different magnetic field distributions (shown in Fig. 5). Note that as the field structure changes between a dipole field and a constant field, flow moves to progressively higher latitudes.

made possible with our FVF model. In the future, we hope to use the model to study wave modes such as the non-zonal MAC waves in more detail to derive constraints on core magnetic field and stratified layer properties and provide insight into many topics including core dynamics, energetics, and many other questions of geophysical significance.

Acknowledgement

This research was supported by grant EAR-1430526 from the National Science Foundation.

Appendix A. Supplementary data

Supplementary data associated with this article can be found, in the online version, athttp://dx.doi.org/10.1016/j.pepi.2018.01.005.

References

Aris, R., 1962. Vectors, Tensors and the Basic Equations of Fluid Mechanics. Printed in USA, London.
Bergman, M.I., 1993. Magnetic Rossby waves in a stably stratified layer near the surface of the Earth's outer core. Geophys. Astrophys. Fluid Dyn. 68 (1–4), 151–176 http://www.tandfonline.com/doi/abs/10.1080/03091929308203566.
Braginsky, S.I., 1993. MAC-oscillations of the hidden ocean of the core. J. Geomagn. Geoelectr. 45, 1517–1538.
Braginsky, S.I., 1998. Magnetic Rossby waves in the stratified ocean of the core, and topographic core-mantle coupling. Earth 50, 641–649 http://adsabs.harvard.edu/cgi-bin/nph-dataquery?bibcode=1998EP%26S50.641B&linktype=ABSTRACT.
Buffett, B.A., 2014. Geomagnetic fluctuations reveal stable stratification at the top of the Earth's core. Nature 507 (7493), 484 http://www.nature.com/nature/journal/v507/n7493/abs/nature13122.html.
Buffett, B.A., Seagle, C.T., 2010. Stratification of the top of the core due to chemical interactions with the mantle. J. Geophys. Res. 115 (B4), B04407 ISSN 0148-0227. http://onlinelibrary.wiley.com/doi/10.1029/2009JB006751/full.
Chulliat, A., Alken, P., Maus, S., 2015. Fast equatorial waves propagating at the top of the Earth's core. Geophys. Res. Lett http://onlinelibrary.wiley.com/doi/10.1002/2015GL064067/full.
Ferziger, J.H., Peric, M., 2002. Computational Methods for Fluid Dynamics.
Finlay, C.C., Olsen, N., Kotsiaros, S., Gillet, N., Clausen, L.T., 2016. Recent geomagnetic secular variation from Swarm and ground observatories as estimated in the CHAOS 6 geomagnetic field model. Earth Planets Space 1–18.
Gubbins, D., Davies, C.J., 2013. The stratified layer at the core mantle boundary caused by barodiffusion of oxygen, sulphur and silicon. Phys. Earth Planet. Inter http://www.sciencedirect.com/science/article/pii/S0031920112001914.
Hernandez, V., Roman, J.E., Vidal, V., 2005. SLEPc: a scalable and flexible toolkit for the solution of eigenvalue problems. ACM Trans. Math. Softw. 31 (3), 351–362.
Hide, R., 1966. Free hydromagnetic oscillations of the Earth's core and the theory of the geomagnetic secular variation. Philos. Trans. R. Soc. A 259 (1107), 615–647 http://rsta.royalsocietypublishing.org/cgi/doi/10.1098/rsta.1966.0026.
Holme, R., Whaler, K.A., 2001. Steady core flow in an azimuthally drifting reference frame. Geophys. J. Int. 145 (2), 560–569.
Hori, K., Jones, C.A., Teed, R.J., 2015. Slow magnetic Rossby waves in the Earth's core.
Jackson, A., Jonkers, A.R.T., Walker, M.R., 2000. Four centuries of geomagnetic secular variation from historical records. Philos. Trans. Math. Phys. Eng. Sci. 358 (1768), 957–990 http://rsta.royalsocietypublishing.org/content/roypta/358/1768/957.full.pdf.
Jones, C.A., 2011. Planetary magnetic fields and fluid dynamos. Annu. Rev. Fluid Mech. 43 (1), 583–614 http://www.annualreviews.org/doi/10.1146/annurev-fluid-122109-160727.
Jones, E., Oliphant, T., Peterson, P., Others, 2001. SciPy: Open Source Scientific Tools for Python. http://www.scipy.org/.
Lesur, V., Whaler, K., Wardinski, I., 2015. Are geomagnetic data consistent with stably stratified flow at the core-mantle boundary? Geophys. J. Int. 201, 929–946.
Livermore, P., Hollerbach, R., Finlay, C., 2016. An accelerating high-latitude jet in Earth's core. Nat. Geosci. 10 (January). http://www.nature.com/doifinder/10.1038/ngeo2859.
Márquez-Artavia, X., Jones, C.A., Tobias, S.M., 2017. Rotating magnetic shallow water waves and instabilities in a sphere. Geophys. Astrophys. Fluid Dyn. 111 (4), 282–322 https://www.tandfonline.com/doi/full/10.1080/03091929.2017.1301937.
Platzman, G.W., 1968. The Rossby wave. Q. J. R. Meteorol. Soc. 94 (401), 225–248 http://onlinelibrary.wiley.com/doi/10.1002/qj.49709440102/abstract.
Roberts, P.H., King, E.M., 2013. On the genesis of the Earth's magnetism. Rep. Prog. Phys.
Schaeffer, N., Jault, D., Nataf, H.-C., Fournier, A., 2017. Turbulent geodynamo simulations: a leap towards Earth's core. Geophys. J. Int. 211 (1), 1–29. http://dx.doi.org/10.1093/gji/ggx265.
Tanaka, S., 2007. Possibility of a low P-wave velocity layer in the outermost core from global SmKS waveforms. Earth Planet. Sci. Lett. 259 (3–4), 486–499 http://linkinghub.elsevier.com/retrieve/pii/S0012821X07002993.
Van Der Walt, S., Colbert, S.C., Varoquaux, G., 2011. The NumPy array: a structure for efficient numerical computation. Comput. Sci. Eng. 13 (2), 22–30.
Vidal, J., Schaeffer, N., 2015. Quasi-geostrophic modes in the Earth's fluid core with an outer stably stratified layer. Geophys. J. Int. 202 (3), 2182–2193.
Whaler, K.A., 1980. Does the whole of the Earth's core convect? http://www.nature.com/nature/journal/v287/n5782/abs/287528a0.html.